Characterization of the MPS I-H knock-in mouse reveals increased femoral biomechanical integrity with compromised material strength and altered bone geometry

Arin K. Oestreich [a,1], Mekka R. Garcia [b,1], Xiaomei Yao [c], Ferris M. Pfeiffer [d], Sabah Nobakhti [e], Sandra J. Shefelbine [e], Yong Wang [c], Amanda C. Brodeur [f], Charlotte L. Phillips [b,g,*]

[a] Department of Biological Sciences, University of Missouri, Columbia, MO 65211, United States
[b] Department of Biochemistry, University of Missouri, Columbia, MO 65211, United States
[c] Department of Oral and Craniofacial Sciences, School of Dentistry, University of Missouri-Kansas City, Kansas City, MO 64108, United States
[d] Department of Orthopaedic Surgery and Bioengineering, University of Missouri, Columbia, MO 65211, United States
[e] Department of Mechanical and Industrial Engineering, Northeastern University, Boston, MA 02115, United States
[f] Department of Biomedical Sciences, Missouri State University, Springfield, MO 65804, United States
[g] Department of Child Health, University of Missouri, Columbia, MO 65211, United States

ARTICLE INFO

ABSTRACT

Mucopolysaccharidosis type I (MPS I), is an autosomal recessive lysosomal storage disorder caused by a deficiency in the α-L-iduronidase enzyme, resulting in decreased enzymatic activity and accumulation of glycosaminoglycans. The disorder phenotypically manifests with increased urine glycosaminoglycan excretion, facial dysmorphology, neuropathology, cardiac manifestations, and bone deformities. While the development of new treatment strategies have shown promise in attenuating many symptoms associated with the disorder, the bone phenotype remains unresponsive. The aim of this study was to investigate and further characterize the skeletal manifestations of the *Idua*-W392X knock-in mouse model, which carries a nonsense mutation corresponding to the IDUA-W402X mutation found in Hurler syndrome (MPS I-H) patients. μCT analysis of the microarchitecture demonstrated increased cortical thickness, trabecular number, and trabecular connectivity along with decreased trabecular separation in the tibiae of female homozygous *Idua*-W392X knock-in (IDUA$^{-/-}$) mice, and increased cortical thickness in male IDUA$^{-/-}$ tibiae. Cortical density, as determined by μCT, and bone mineral density distribution, as determined by quantitative backscattered microscopy, were equivalent in IDUA$^{-/-}$ and wildtype (Wt) bone. However, tibial porosity was increased in IDUA$^{-/-}$ cortical bone. Raman spectroscopy results indicated that tibiae from female IDUA$^{-/-}$ had decreased phosphate to matrix ratios and increased carbonate to phosphate ratios compared to Wt female tibiae, whereas these ratios remained equivalent in male IDUA$^{-/-}$ and Wt tibiae. Femora demonstrated altered geometry and upon torsional loading to failure analysis, female IDUA$^{-/-}$ mouse femora exhibited increased torsional ultimate strength, with a decrease in material strength relative to Wt littermates. Taken together, these findings suggest that the IDUA$^{-/-}$ mutation results in increased bone torsional strength by altering the overall bone geometry and the microarchitecture which may be a compensatory response to increased porosity, reduced bone tensile strength and altered physiochemical composition.

1. Introduction

Mucopolysaccharidosis type I (MPS I; MIM# 252800) is an autosomal recessive lysosomal storage disorder caused by a deficiency in the lysosomal enzyme α-L-iduronidase (EC 3.2.1.76), which catalyzes the degradation of the glycosaminoglycans (GAGs), dermatan sulfate and heparan sulfate [1]. The clinical severity of MPS I is dependent upon α-L-iduronidase activity, which can vary widely and has been categorized into three distinct phenotypic subtypes: MPS I-Hurler (MPS I-H; MIM# 607014), MPS I-Scheie (MPS I-S; MIM# 607016), and MPS I-

Hurler/Scheie (MPS I-H/S; MIM# 607015), with the clinical severity ranging from MPS I-H being the most severe subtype to MPS I-S being the least severe. The incidence of MPS I-H is estimated to occur in 1:100,000 births [2]. The accumulation of GAGs results in progressive cellular damage and visual impairment, hearing loss, cardiac manifestations, organomegaly, developmental delay with subsequent progressive cognitive decline initiated by age 2 in severe MPS I-H patients [3]. Furthermore, MPS I-H patients present with severe skeletal abnormalities through poorly understood mechanisms [4]. The skeletal abnormalities are collectively known as dysostosis multiplex, and consist of stiffness and contracture of joints, enlarged skull, genu valgum, thoracolumbar kyphosis, hip dysplasia, abnormally shaped vertebrae and ribs, hypoplastic epiphyses and short stature [5–8]. As a result of the skeletal manifestations, MPS I-H patients typically undergo multiple high-risk surgical interventions to delay the progression of the skeletal disease and improve quality of life [9–11]. Novel therapeutic treatments such as bone marrow or umbilical cord blood transplantation and weekly enzyme replacement are currently being used to sustain overall enzyme activity and have improved and extended the quality of life of Hurler patients. However, these treatments are unable to fully prevent development of the skeletal manifestations in Hurler patients [9,12]. Therefore, despite these therapeutic gains, MPS-I patients continue to endure the consequences of disabling, painful bone disease that often require rigorous surgical intervention.

In contrast to the two previously reported *Idua* knock-out mouse models, *Idua* −/− and MPS I [13,14], the *Idua*-W392X knock-in mouse model carries a nonsense mutation corresponding to the *IDUA*-W402X mutation, commonly found in Hurler syndrome patients [15]. Wang et al. showed that the phenotype of *Idua*-W392X mouse model parallels that of human MPS I-H disease, which includes GAG accumulation due to loss of α-L-iduronidase activity, cardiac manifestations and bone abnormalities such as broadening of the face, thickening of the zygomatic arch and atypical femur length and width [15]. Even though the existing animal models have been useful in evaluating various therapeutic approaches such as enzyme replacement therapy [16], bone marrow transplantation [17,18], and gene therapy [19,20], much of the molecular mechanisms leading to the pathology remain to be elucidated. Although it has been shown that the *Idua*-W392X presents with typical skeletal findings of MPS I-H [15,21], the whole bone biomechanical and material properties have not been evaluated. The paucity in understanding the pathogenic mechanisms responsible for the musculoskeletal manifestations likely contributes to the absence of improvement in the bone phenotype with the current therapies.

The goal of this study was to evaluate the microarchitecture, physiochemical composition and biomechanical integrity of the *Idua*-W392X knock-in mouse model, in order to better define the underlying biomechanical properties of the skeletal abnormalities and to begin to elucidate the physiochemical mechanisms. Femora and tibiae from wildtype (Wt), heterozygous *Idua*-W392X (IDUA$^{+/-}$) and homozygous *Idua*-W392X (IDUA$^{-/-}$) 16 week old mice were evaluated on the basis of whole bone biomechanical integrity and material properties. This study highlights the microarchitectural, physiochemical, and biomechanical basis of the MPS I-H skeletal phenotype and can be used to drive forward the design and improvement of current and future therapies to improve the bone quality of MPS I-H patients.

2. Methods

2.1. Animals and tissue harvest

The *Idua*-W392X mice were a generous gift from Dr. Kim Keeling, University of Alabama at Birmingham, Alabama [15]. *Idua*-W392X mice were previously backcrossed into a C57BL/6J congenic background [17]. IDUA$^{+/-}$ breeding pairs and their offspring were housed in an AAALAC accredited facility at the University of Missouri-Columbia and had ad libitum access to water and food (Purina 5008 Formulab Diet;

Purina Mills Inc., St. Louis, MO). This study was performed under an approved University of Missouri Animal Care and Use Protocol. The breeders and offspring were genotyped as previously described [17] and weighed weekly starting at 5 weeks of age. The mice were raised to 16 weeks of age (peak bone mineral density [22]), sacrificed, and femora and tibiae were excised, the soft tissue removed, and the bones wrapped in sterile 1× PBS soaked gauze and stored at −20 °C until analyzed.

2.2. Tibial microarchitecture analysis

The macro- and microarchitecture of the left tibiae was determined by microcomputed tomography (μCT) with the vivaCT 40 (Scanco Medical AG, Bassersdorf, Switzerland) as previously described [23] using 55 kVp X-ray tube potential, 145 μA current, 10 μm voxel resolution, and 200 ms integration time to assess cortical bone and trabecular bone properties. By hydroxyapatite calibration, the voxel values were converted to a mineral-equivalent value, milligrams per cubic centimeter (mg/cm^3). Three dimensional images of the tibiae were reconstructed along the long axis with series of 10 μm-thick slices, using a global threshold of 253 (μCT gray value). The tibial cortical density and thickness were evaluated in the transverse plane at the mid-shaft starting 1 mm proximal to the fibula–tibia junction. The proximal metaphysic trabecular bone was analyzed 1 mm below the growth plate, and the following determined: the bone volume fraction (BV/TV), trabecular bone density, thickness, number, separation, connectivity density, which describes abundance of trabecular connections, and the structure model index (SMI), which describes shape of individual trabecular bone ranging from 0 (perfect plate) to 3 (cylindrical rods) [24,25].

2.3. Tibial bone mineral density distribution and porosity

Quantitative backscattered scanning electron microscopy of left tibias was used to characterize the bone mineral density distribution (BMDD) and porosity. Tibiae were scanned in a digital electron microscope containing a four-quadrant semiconductor backscattered detector (Evo, Ziess, Germany). Imaging was performed at a 20 kV accelerating voltage, saturated filament current, 0.5 nA probe current measured with a Faraday cup and a working distance of 12 mm. Magnification settings, store resolution and scan speed were kept consistent between different imaging sessions to result in a pixel size of 760 nm. Several high magnification images were taken from the cross section of each sample and the images were combined using an image processing software (Image composite editor, Microsoft Research) to form the whole bone cross section. To calibrate the backscattered signal, pure carbon and aluminum standards (Micro-Analysis Consultants, UK) were imaged in each scan and at the same condition of imaging the bone. Calibration standards were imaged in several intervals while scanning the bone. After imaging, the graylevel numbers of standards were averaged between each two subsequent images of the phantom to account for the signal variations. In a post-processing analysis and to keep the scale of the graylevel histograms consistent between images, graylevel numbers of the bone and phantom were expanded linearly such that carbon and aluminum were 25 and 225, respectively. A histogram containing the incidence of graylevel numbers was calculated for each sample and the mode and the full width at half maximum (FWHM) of the histograms were determined. The bone porosity was determined by excluding regions with cracks and microcracks from the bone cross-section and then determining the fraction of the bone area with lacunae and blood vessels relative to the total bone area (Fig. 3A–C).

2.4. Bone mineral and matrix composition

Following μCT analyses the left tibia was sliced across the diaphyseal midshaft and the cortical bone cross-sections were evaluated by Raman

spectroscopy using a LabRam HR 800 Raman spectrometer (Horiba JobinYvon, Edison, NJ). Raman spectroscopy uses molecular vibrational techniques to evaluate the chemical properties (structure and composition) of the mineral and organic matrix components of bone. Averaged bone biochemical composition was determined from Raman spectra (700 to 1800 cm^{-1} range) that were excited by a helium-neon laser (633 nm) with a 50× water immersion objective as previously described [23], allowing acquisition of peaks attributed to the bone minerals and proteins. For each tibia the midshaft cortical cross-section was examined at 4 points (anterior, posterior, medial and lateral) and the data averaged for each sample. Spectra analyses were performed to measure the area of hydroxyapatite ν_1 PO_4^{3-} peak (960 cm^{-1}), type B ν_1 CO_3^{2-} peak (1070 cm^{-1}), and matrix CH_2 band (1450 cm^{-1}) and amide I [23]. The ratios of carbonate/phosphate (CO_3^{2-}/PO_4^{3-}), mineral to matrix (PO_4^{3-}/CH_2), and mineral to collagen ($PO_4^{3-}/amide$ I) were assessed.

2.5. Femoral μCT and torsional loading to failure

Prior to bone biomechanical testing, the right femoral geometric parameters were evaluated by μCT analyses (MicroCAT II, Siemens Medical). The image slices were reconstructed using the Amira 5.3.3 software package (Mercury Computer Systems/TGS) as previously described [23] to give a cubic voxel dimension of 0.083 mm^3. The mid-shaft slice was modeled as a hollow elliptical cross-section with periosteal ($_p$) and endosteal ($_e$) anterior–posterior (d_p and d_e; minor diameters) and medio-lateral (D_p and D_e; major diameters, and q = D_e / D_p). Each femora was potted into a customized single use holder with an exposed femur test length of 7 mm, and then subjected to torsional loading to failure analyses as previously described using the TA-HDi testing machine (Stable Micro Systems, Surrey, UK) [23]. Applied torque T (Nmm) was determined and evaluated as a function of relative angular displacement θ (degrees) (Fig. 6A). The whole bone parameters, torsional ultimate strength (T_{max}, Nmm), strain energy to failure (U, Nmm) and torsional stiffness (Ks, Nmm/rad), take into account both the material the bone is comprised of and the size and shape of the bone. The bone material properties, tensile strength (Su, N/mm^2; Su = $[16T_{max} / (\pi D_p d_p^2 (1 - q^4))]$) and shear modulus of elasticity, (G, N/mm^2; shear modulus of elasticity = torsional stiffness × 7 mm / polar moment of area), were assessed as previously described [23].

2.6. Statistical analysis

All statistical analyses were performed using SAS (SAS Institute Inc., Cary, NC). Growth curves quantifying body weight were analyzed as a repeated measures design (split plot and time) as outlined by Littell et al. [26]. The fixed effects were arranged as a 3 × 2 × 12 factorial (3 genotypes × 2 sexes × 12 time points). The genotype, sex, and genotype × sex interactions represent the main plot, and time and all possible interactions with the main plot represent the subplot. The denominator of F for the main plot effect was the random effect, mouse ID per given genotype and sex. The residual mean square was used to test all subplot effects. Since this was a three-way interaction the differences between genotypes were tested for the two sexes keeping time constant.

Bone microarchitecture, geometric parameters, and biomechanical properties were evaluated by analysis of covariance with body weight as the covariate, and the physiochemical parameters were evaluated by analysis of variance by a 3 × 2 factorial (3 genotypes and 2 sexes). Specifically, mean differences were determined using Fisher's Protected Least Significant Difference [27]. Fisher's Protected Least Significant Difference permits most comparisons to be orthogonal (independent) using a contrast statement. Six preplanned pairwise comparisons were analyzed. When heterogeneous variations made it necessary (p ≤ 0.05 as determined by Bartlett's test for homogeneity), a log transformation was used to stabilize the variation. If the log transformation failed to

stabilize the variation, a non-parametric ranked analysis was performed according to Conover et al. [28]. Data are presented as mean ± standard error (SE). Differences were considered to be statistically significant at p ≤ 0.05.

3. Results

3.1. Growth curves

Both male and female IDUA$^{-/-}$ mice were inherently heavier than their Wt and IDUA$^{+/-}$ littermates at 16 weeks of age (Fig. 1). Growth curves indicated that male IDUA$^{-/-}$ mice began to diverge from their Wt and IDUA$^{+/-}$ littermates at 10 weeks of age (Fig. 1A). Female IDUA$^{-/-}$ mice also began to diverge from their Wt littermates at 10 weeks, but did not become significantly heavier than their IDUA$^{+/-}$ littermates until 16 weeks of age (Fig. 1B). Sex-matched Wt and IDUA$^{+/-}$ littermates had similar weights at 16 weeks of age (Fig. 1). These findings were consistent with the previous study by Russell et al. [29]. In order to determine if the effect of the *Idua-W392X* mutation on the bone is independent of the increase in body weight, the following microarchitecture, geometric, and biomechanical data were evaluated by analysis of covariance with body weight as the covariate.

3.2. Microarchitecture

Evaluation of the skeletal microarchitecture determined that tibiae from female IDUA$^{-/-}$ mice had increased cortical thickness (Table 1), as well as increased trabecular number (Fig. 2D) and connectivity density (Fig. 2F), and a subsequent decrease in trabecular separation (Fig. 2E) compared to their Wt and IDUA$^{+/-}$ littermates. Sixteen week old male IDUA$^{-/-}$ tibiae exhibited similar trends, but only cortical thickness reached significance (Table 1). The tibiae of IDUA$^{+/-}$ mice were equivalent to Wt littermates for the majority of the bone parameters, except IDUA$^{+/-}$ females showed an increase in cortical density, and IDUA$^{+/-}$ males showed an increase in trabecular density when compared to Wt counterparts (Table 1). Genotype related changes in trabecular density, thickness, or SMI were not observed at 16 weeks of age (Table 1). These data suggest that the IDUA$^{-/-}$ mutation alters both the cortical and trabecular bone microarchitecture and appears to be more pronounced in female mice.

3.3. Cortical density and porosity

Quantitative back-scattered electron microscopy was used to evaluate the bone mineral density distribution (BMDD) at mid-diaphysis of the mouse tibia. In bone, atomic number of the matrix is related to the calcium content and therefore, areas which contain a higher concentration of calcium had a higher graylevel number, which for the Wt, IDUA$^{+/-}$, and IDUA$^{-/-}$ images (Fig. 3A, B & C) is indicated in orange to red and the regions with the least mineralization (Lacunae and osteoid) are represented by the lower graylevel number and the color blue. By quantitative backscattered scanning electron microscopy the BMDD of female Wt and IDUA$^{-/-}$ tibias was equivalent (Fig. 3E–F), confirming the μCT cortical density findings (Table 1). Tibial porosity was defined and calculated as the area of pores (blue) divided by the area of the bone. The quantification indicated IDUA$^{-/-}$ tibial cortical bone porosity was 50% greater than Wt, while the cortical porosity of the IDUA$^{+/-}$ tibias were 12.2% greater than age and sex matched Wt littermates (Fig. 3G).

3.4. Material composition

To investigate the material and physiochemical properties of the cortical bone, Raman spectroscopy was performed to quantify specific components: phosphate (PO_4^{3-}), carbonate (CO_3^{2-}), matrix (CH_2) and collagen (amide I). Tibiae from male Wt, IDUA$^{+/-}$, and IDUA$^{-/-}$ mice
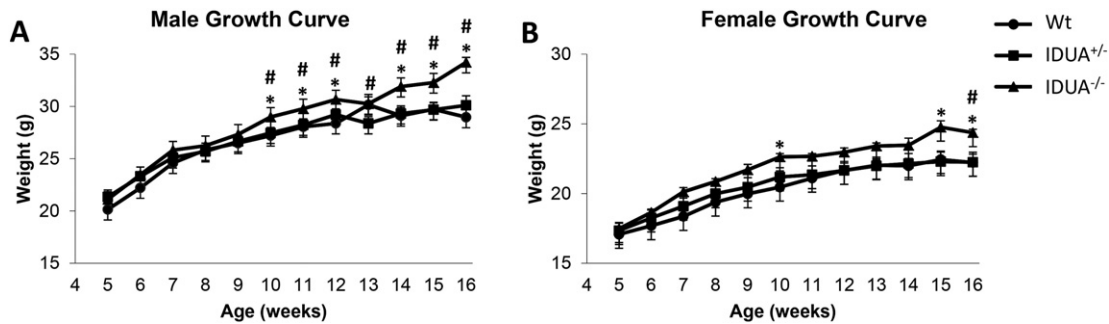
Fig. 1. Weekly weighing demonstrated that A) male and B) female IDUA$^{-/-}$ (*triangle*) mice exhibited increased body weight compared to their Wt (*circle*) and IDUA$^{+/-}$ (*square*) littermates at 16 weeks of age. Mice were weighed weekly from 5–16 weeks of age. Values are the means of sex and genotype specific groups. * denotes IDUA$^{-/-}$ weight difference compared to sex-matched Wt littermates and # denotes IDUA$^{-/-}$ weight difference compared to sex matched IDUA$^{+/-}$ littermates. Differences were considered significant at p ≤ 0.05. Male Wt [week 5 (n = 6), weeks 6–16 (n = 10)], IDUA$^{+/-}$ [weeks 5–7 (n = 8), weeks 8–12 (n = 10), weeks 13–15 (n = 11), week 16 (n = 9)], and IDUA$^{-/-}$ [week 5 (n = 5), weeks 6–7 (n = 6), weeks 8–15 (n = 8), week 16 (n = 6)]; female Wt [week 5 (n = 8), weeks 6–7 (n = 9), weeks 8–12 (n = 11), weeks 13–15 (n = 12), week 16 (n = 10), IDUA$^{+/-}$ [week 5 (n = 14), weeks 6–16 (n = 15)], and IDUA$^{-/-}$ [week 5 (n = 4), weeks 6–16 (n = 6)].

did not show differences in material composition (Fig. 4). However, female IDUA$^{-/-}$ tibias exhibited increases in the carbonate/phosphate (CO_3^{2-}/PO_4^{3-}) ratio (Fig. 4A) and decreases in phosphate/matrix (PO_4^{3-}/CH_2) (Fig. 4B), and had a lower phosphate:collagen (PO_4^{3-}/amide I) ratio compared to Wt littermates, although it did not reach significance (p = 0.0647) (Fig. 4C). The phosphate:matrix and phosphate:collagen ratios of female IDUA$^{-/-}$ tibias were decreased compared to IDUA$^{+/-}$ littermates, as well, which were similar in composition to Wt.

3.5. Femoral geometry and biomechanical strength

Bone strength is cumulatively dictated by the interplay of the bone geometry and the composition of the bone material. To determine if the changes observed in bone microarchitecture and material properties altered the whole bone strength in IDUA$^{-/-}$ mice, we subjected femora from male and female Wt, IDUA$^{+/-}$ and IDUA$^{-/-}$ mice to μCT and torsional loading to failure. Both male and female IDUA$^{-/-}$ mice had shorter femurs with 16% and 14% larger midshaft marrow diameters and 9% and 14% greater cortical bone widths compared to sex-matched Wt littermates, respectively (Fig. 5), which was consistent with our observations of increased cortical thickness in the tibia (Table 1). Male and female IDUA$^{-/-}$ femora both showed an increase of 75% in their polar moment of area (a geometric predictor of increased bone strength) as compared to sex-matched Wt littermates (Fig. 5). Male and female Wt femora exhibit equivalent values for all the geometric parameters as sex-matched IDUA$^{+/-}$ femora. Femoral geometry differences between sexes were observed in cortical bone width of Wt mice, and the polar moment of area of Wt and IDUA$^{+/-}$ mice (Fig. 5).

To evaluate if the changes in bone microarchitecture, physiochemical composition, and geometry altered the overall strength of the IDUA$^{-/-}$ bone, femora were subjected to torsional loading to failure. Female IDUA$^{-/-}$ femora exhibited 30.8% increase in energy to failure, the

amount of energy the bone absorbed prior to fracture, relative to Wt femora (Fig. 6B). Male IDUA$^{-/-}$ femora showed a 16.2% increase in energy to failure relative to Wt, although did not reach significance (Fig. 6B). Torsional ultimate strength (T$_{max}$) is a whole bone property that measures the maximum amount of torque required to break the bone. Femora from both male and female IDUA$^{-/-}$ mice exhibited increased T$_{max}$ compared to their Wt and IDUA$^{+/-}$ littermates. Tensile strength, a measure of the strength of the bone material, was decreased by 23.8% in female IDUA$^{-/-}$ femora as compared to Wt (Fig. 6D). In male IDUA$^{-/-}$ mice, the femoral tensile strength was reduced 19.7% as compared to Wt, however, the trend did not reach significance (p = 0.10). The torsional stiffness was not impacted by genotype (Fig. 6E). However, shear modulus of elasticity, a measure of the stiffness of the bone material, was decreased in femora from IDUA$^{-/-}$ females compared to their Wt and IDUA$^{+/-}$ littermates (Fig. 6F). These data suggest that the increased whole bone strength observed in femora of IDUA$^{-/-}$ mice results from changes in the microarchitecture, geometry and the bone material properties. While the changes in bone geometry are predicted to increase strength, the changes in material properties appear detrimental. Taken together, the impact of the absence of α-L-iduronidase activity on the biomechanical integrity of the whole bone is the result of opposing forces of the impact of geometry and bone material properties to produce an overall increase in torsional strength. The IDUA bone is in a delicate balance of trying to maintain skeletal integrity in the presence of compromised bone material.

4. Discussion

Although enzyme replacement and stem cell therapies for treating MPS I have been effective in attenuating organomegaly, cardiac, respiratory and neurological symptoms of the lysosomal storage disorder MPS I, the musculoskeletal manifestations are recalcitrant to current treatment strategies [9,11,17,30,31]. The goal of this study was to fully

Table 1
Tibial microarchitecture of 16 week old male and female Wt, IDUA$^{+/-}$ and IDUA$^{-/-}$ mice.

	Male			Female		
	Wt n = 5	IDUA$^{+/-}$ n = 5	IDUA$^{-/-}$ n = 4–5	Wt n = 3	IDUA$^{+/-}$ n = 4	IDUA$^{-/-}$ n = 5
Cortical density (mg HA/CCM)	1139.81 ± 11.91	1123.46 ± 13.45	1119.25 ± 3.52	1112.90 ± 8.42	1142.28 ± 8.42[a]	1118.86 ± 9.86[b]
Cortical thickness (mm)	0.210 ± 0.005	0.207 ± 0.003	0.250 ± 0.09[a,b]	0.195 ± 0.004	0.195 ± 0.001	0.237 ± 0.006[a,b]
Trabecular density (mg HA/CCM)	890.93 ± 21.90	930.08 ± 4.62[a]	927.86 ± 8.88	889.53 ± 8.30	896.47 ± 2.10	908.12 ± 6.78
Trabecular BV/TV (%)	0.227 ± 0.030	0.228 ± 0.020	0.217 ± 0.031	0.077 ± 0.008	0.075 ± 0.007	0.170 ± 0.021
Trabecular Thickness (mm)	0.053 ± 0.004	0.054 ± 0.003	0.049 ± 0.003	0.041 ± 0.001	0.041 ± 0.001	0.047 ± 0.003
Trabecular SMI	1.607 ± 0.310	1.76688 ± 0.199	1.961 ± 0.227	3.026 ± 0.085	2.789 ± 0.135	2.139 ± 0.123

[a] p ≤ 0.05 compared to Wt.
[b] p ≤ 0.05 compared to IDUA$^{+/-}$.
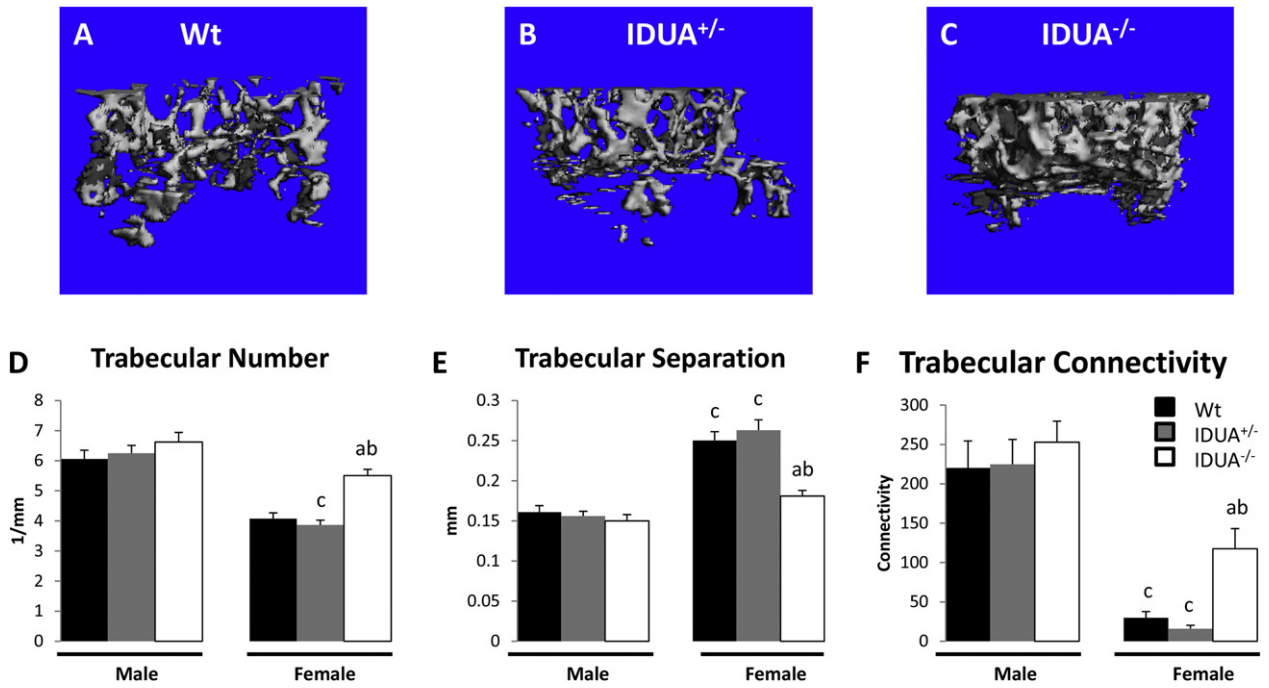
Fig. 2. Trabecular microarchitecture of male and female tibiae as determined by μCT. Representative images of A) Wt, B) IDUA$^{+/-}$, and C) IDUA$^{-/-}$ μCT scans. D) Trabecular number was increased in IDUA$^{-/-}$ tibiae (*white bar*) compared to sex-matched Wt (*black bar*) and IDUA$^{+/-}$ (*gray bar*) littermates. E) Trabecular separation was decreased in IDUA$^{-/-}$ females compared to sex-matched Wt and IDUA$^{+/-}$ littermates. F) Trabecular Connectivity was increased in IDUA$^{-/-}$ females compared to sex-matched Wt and IDUA$^{+/-}$. Values are means ± SE. [a]$p \leq 0.05$ compared to sex-matched Wt, [b]$p \leq 0.05$ compared to sex-matched IDUA$^{+/-}$, [c]$p \leq 0.05$ compared to genotype-matched male. Male Wt (n = 5), IDUA$^{+/-}$ (n = 5), and IDUA$^{-/-}$ (n = 4); Female Wt (n = 5), IDUA$^{+/-}$ (n = 4), and IDUA$^{-/-}$ (n = 5).
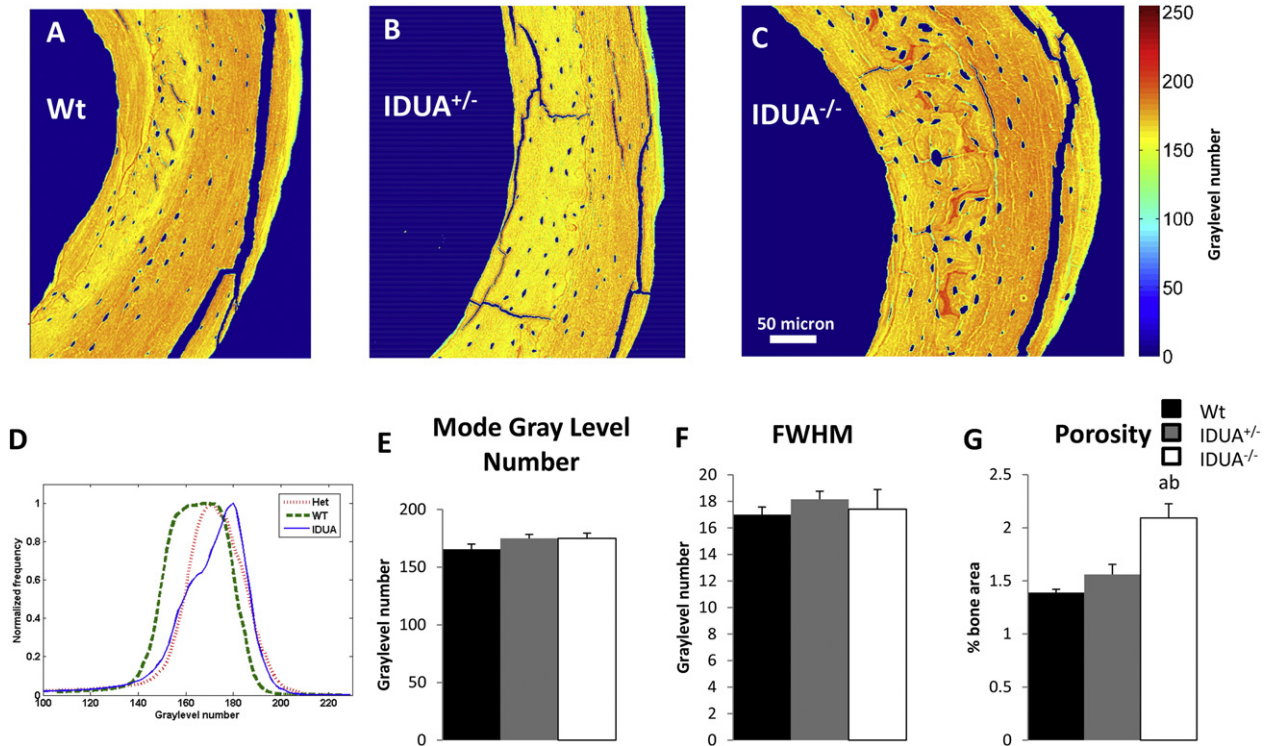
Fig. 3. Bone mineral density distribution (BMDD) and porosity analysis as determined by scanning electron microscopy. Representative segments of female A) Wt, B) IDUA$^{+/-}$, and C) IDUA$^{-/-}$ cross-sectional BMDD images of the medial section of the mid-diaphysis of the tibia (range of 256 graylevel numbers, with red representing the greatest density of calcium and blue the least). For each sample the whole cross-sectional image was used to determine the BMDD histogram. D) Summation of all the histograms for each group shown based on the frequency of graylevel numbers divided by the maximum frequency in each case. E) Averaged mode of graylevel histograms and F) the averaged full width at half maximum (FWHM) values extracted from graylevel histograms were not different between genotypes. G) Porosity quantification of Wt (*black bar*), IDUA$^{+/-}$ (*gray bar*) and IDUA$^{-/-}$ (*white bar*) showing an increase in porosity in the IDUA$^{-/-}$ tibiae. Values are means ± SE. [a]$p \leq 0.05$ compared to sex-matched Wt, [b]$p \leq 0.05$ compared to sex-matched IDUA$^{+/-}$. Wt (n = 5), IDUA$^{+/-}$ (n = 5), and IDUA$^{-/-}$ (n = 4).
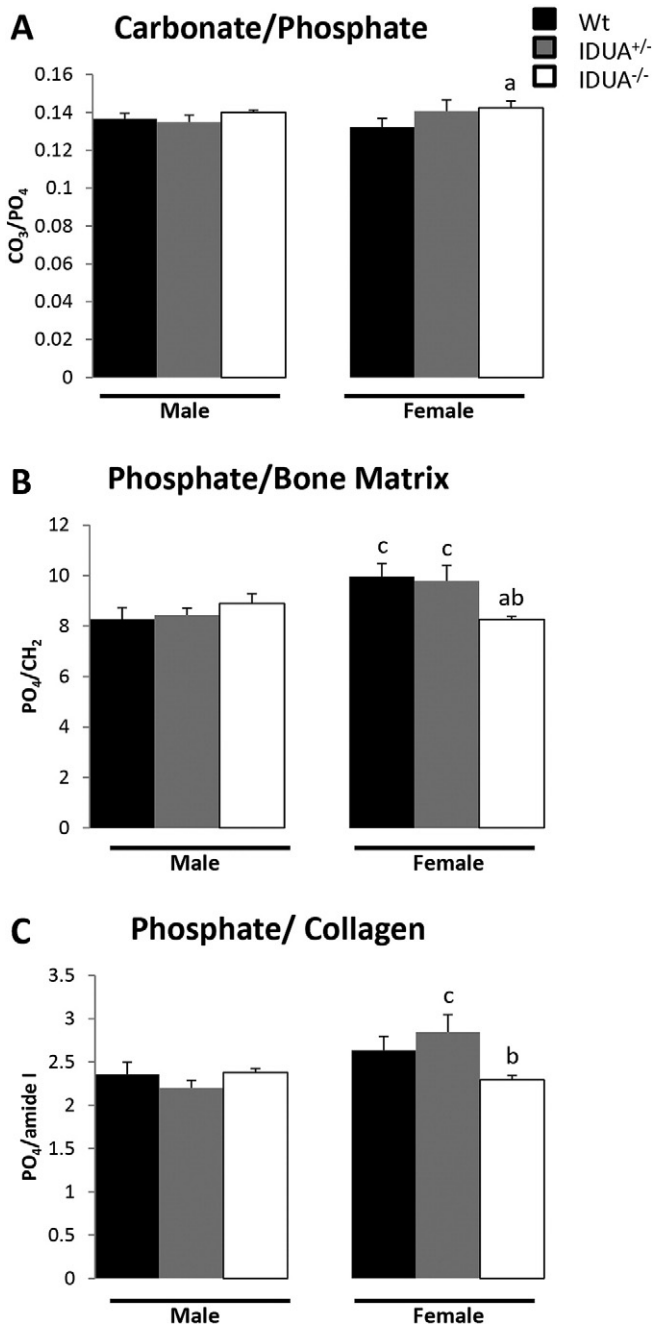
Fig. 4. Physiochemical composition of the tibial cortical bone was determined using Raman spectroscopy. A) Carbonate/phosphate ratios [(CO_3^{2-}/PO_4^{3-}); indication of carbonate substitution of phosphate in the crystal lattice] were increased in tibiae from IDUA$^{-/-}$ females (*white bar*) compared to Wt (*black bar*). B) Phosphate to bone matrix ratios [(PO_4^{3-}/CH_2); indication of the relative amount of mineral phosphate to organic matrix] was decreased in tibiae from IDUA$^{-/-}$ females compared to Wt and IDUA$^{+/-}$ (*gray bar*) littermates of the same sex. C) Phosphate to collagen ratios [(PO_4^{3-}/amide I); indication of the relative amount of phosphate mineral to collagen] was decreased in tibiae from female IDUA$^{-/-}$ compared to IDUA$^{+/-}$ littermates and had a decreased trend compared to sex-matched Wt littermates ($p = 0.06$). Values are means $\pm$ SE. [a]$p \leq 0.05$ compared to sex-matched Wt, [b]$p \leq 0.05$ compared to sex-matched IDUA$^{+/-}$, [c]$p \leq 0.05$ compared to genotype-matched male. Male Wt ($n = 5$), IDUA$^{+/-}$ ($n = 5$), and IDUA$^{-/-}$ ($n = 4$); Female Wt ($n = 5$), IDUA$^{+/-}$ ($n = 4$), and IDUA$^{-/-}$ ($n = 5$).

characterize the skeletal geometry, microarchitecture, biomechanical and physiochemical properties of the *Idua-W392X* knock-in (IDUA$^{-/-}$) mouse model of MPS I in order to better understand the consequences of α-L-iduronidase enzyme deficiency and subsequent accumulation of GAGs to skeletal integrity. Our findings suggest that complete absence of α-L-iduronidase results in changes not only to the macro- and

microarchitecture of cortical and trabecular bone, but also to the physiochemical composition and porosity. These changes while opposing, ultimately culminate in an overall increase in whole bone strength. As anticipated with autosomal recessive metabolic disorders, the IDUA$^{+/-}$ mice were primarily unaffected and the skeletal integrity of their long bones was equivalent to their Wt littermates.

It has been repeatedly demonstrated that patients with Hurler syndrome have decreased growth velocity and short stature which persists following hematopoietic stem cell replacement therapy [32]. Both parameters contribute to and are indirect measures of the pathologic and biochemical alterations seen in Hurler syndrome. Our study demonstrates that the IDUA$^{-/-}$ mice have decreased femur length and are heavier than Wt and IDUA$^{+/-}$ littermates at 16 weeks of age, as has been seen in untreated human patients, and previously in IDUA$^{-/-}$ mice [15,21] as well as other mouse models of MPS [29,33,34]. It is likely that the decreased height observed in Hurler syndrome patients may be attributed to abnormalities in the growth plate caused by GAG accumulation [29,35,36]. The growth plates of IDUA$^{-/-}$ femora were shown to have a 4-fold increase in osteoclast activity by tartrate-resistant acid phosphatase histochemistry relative to wildtype femora [21]. Wilson et al. demonstrated that *Idua* −/− knock-out mouse tibiae had twice as much cartilage in the subepiphyseal zone of the growth plate, reduced type II collagen degradation, and ossification as wildtype mouse tibiae [37].

Our analysis of the tibial microarchitecture and geometry in IDUA$^{-/-}$ mice at 16 weeks of age demonstrated increased cortical thickness without changes in cortical density and were consistent with studies in IDUA$^{-/-}$ mice [21], as well as the *Idua* −/− knockout mice, which exhibited decreased femur length with a general thickening as measured by radiography [13,34], and shortening of the tibia length, and increased femoral midshaft diameter without changes in bone mineral density [34]. Additionally, we report an increase in the femoral bone marrow diameter along with microarchitecture changes in the trabecular bone of female IDUA$^{-/-}$ tibias. Consistent with studies in other mouse models of MPS [38], the tibial trabecular bone of female IDUA$^{-/-}$ mice showed an increase in trabecular number and connectivity density with a subsequent decrease in separation which suggests overall increases in bone material and that the bone microarchitecture has been altered by the deficiency in α-L-iduronidase. Studies by Pievani et al. have demonstrated an increase in BV/TV in femora of an *Idua* −/− knockout mouse model for MPS at 37 weeks of age [38], whereas Gunn et al. found that 31 week old male IDUA$^{-/-}$ femora had increased cortical thickness, trabecular BV/TV, number, and connectivity density, and decreased structural model index (SMI) and trabecular separation [21]. When female IDUA$^{-/-}$ tibiae were analyzed using an ANOVA the BV/TV was increased as compared to their sex-matched Wt and IDUA$^{+/-}$ littermates. However, when using body weight as a co-variate the difference was no longer significant (Table 1). This suggests that at 16 weeks, the increase in BV/TV in the tibiae of female IDUA$^{-/-}$ mice can be attributed to a response to an increase in body weight. The compromised bone material and the increased cortical porosity in the IDUA$^{-/-}$ mouse further suggests that these geometric changes and the response of the microarchitecture may function to protect the integrity of the bone and/or simply reflect alterations in bone remodeling.

Previous studies have implicated reductions in osteoclast number and activity in MPS, specifically that the accumulation of MPS-associated GAGs (dermatan sulfate and heparin sulfate) may inhibit the collagenolytic activity and osteoclast function [37] as well as increase the number of osteoblasts in the intertrabecular spaces [29]. However, Gunn et al. reported a 4-fold elevation in osteoclast activity in the growth plates of femurs of 31 week old IDUA$^{-/-}$ mice relative to wildtype femoral growth plates [21]. In a recent study of serum and urine bone formation and resorption biomarkers, Stevenson et al. found that children with MPS had elevated serum osteocalcin levels and trends of increased serum bone specific alkaline phosphatase
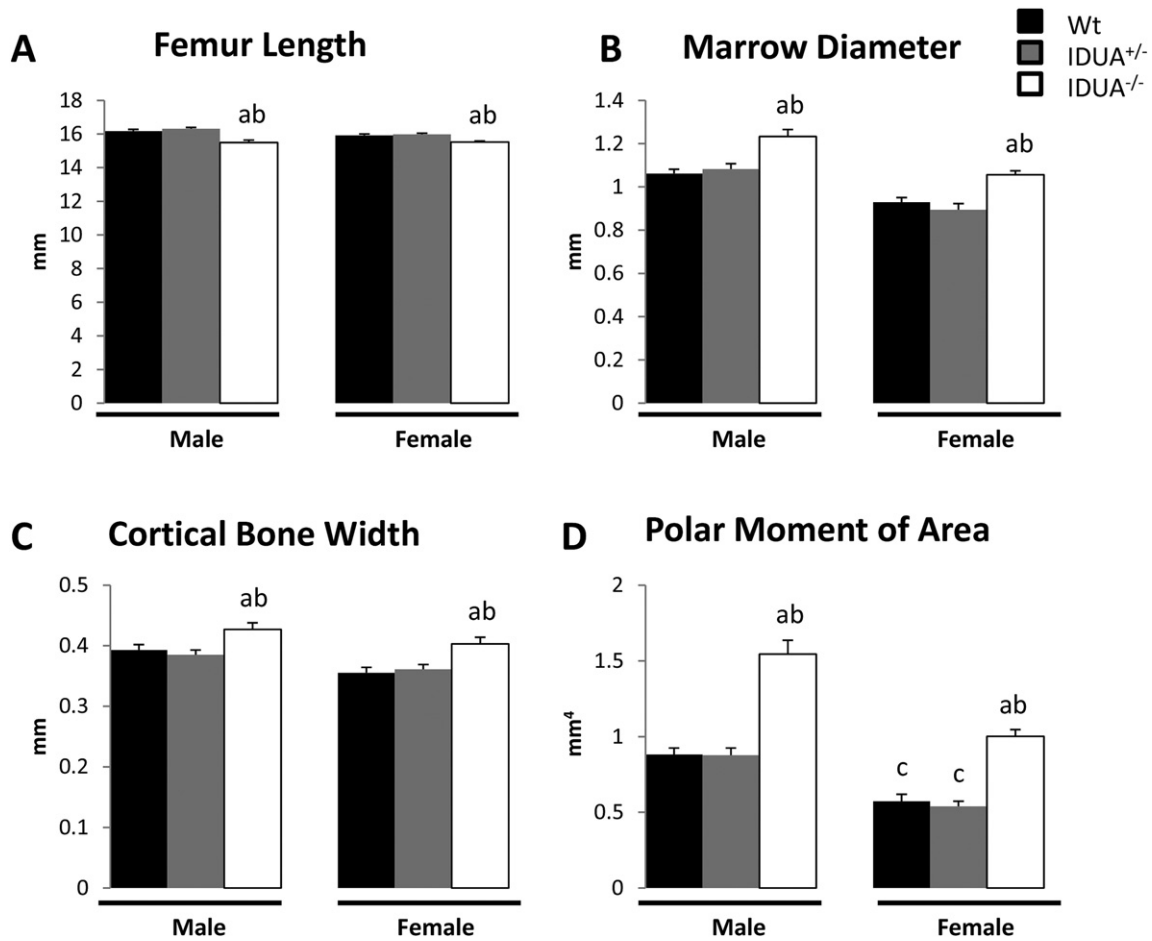
Fig. 5. Geometric parameters and polar moment of area of male and female Wt, IDUA$^{+/-}$, and IDUA$^{-/-}$ femora as determined by μCT. A) Femoral length was decreased, and B) marrow diameter, C) cortical bone width, and D) polar moment of area were increased in IDUA$^{-/-}$ femurs (*white bar*) compared to sex-matched Wt (*black bar*) and IDUA$^{+/-}$ (*gray bar*) femora. Values are means ± SE. [a]p ≤ 0.05 compared to sex-matched Wt, [b]p ≤ 0.05 compared to sex-matched IDUA$^{+/-}$, [c]p ≤ 0.05 compared to genotype-matched male. Male Wt (n = 10), IDUA$^{+/-}$ (n = 9), and IDUA$^{-/-}$ (n = 11); Female Wt (n = 7), IDUA$^{+/-}$ (n = 7), and IDUA$^{-/-}$ (n = 10).

compared to age and tanner-stage matched unaffected children [39], suggesting that children with MPS may have increased osteoblast activity. In the IDUA$^{-/-}$ mice the increased porosity per bone volume is indicative of increased osteocyte lacunae, which potentially reflects increased osteoblasts which likely have compromised function resulting in the formation of poorer quality bone. In addition, the increase in carbonate to phosphate ratios in the female IDUA$^{-/-}$ tibia suggests a more mature matrix and perhaps decreased degradation. Taken together these findings and ours further suggest that the pathogenesis of the musculoskeletal manifestations in MPS is associated with abnormal bone remodeling. Future studies to investigate osteoblast, osteoclast and osteocyte function, bone remodeling efficiency, and dynamic and static histomorphometry are necessary to further elucidate this mechanism.

Bone is a composite of organic matrix and mineral; the mineral component, hydroxyapatite, provides stiffness, while the organic component is 80% collagen, of which 95% is type I collagen [40], and imparts material toughness (the capacity to absorb energy) [41]. Together, the abundance, quality and proportion of these components impact the overall structural integrity of the bone. Bone strength is dependent upon the cumulative contributions of the integrity of the bone material, microarchitecture and geometry. The results of the torsional loading to failure in the IDUA$^{-/-}$ mice revealed an overall increase in strength as measured by the whole bone parameters, torsional ultimate strength and energy to failure, but also compromised bone material strength of the IDUA$^{-/-}$ bone as measured by tensile strength and shear modulus of elasticity. This would suggest that the increase in strength is a net

result of positive alterations in the microarchitecture and geometry of the bone that are able to compensate for the adverse changes in the material and physiochemical composition.

Changes in extracellular matrix components have been implicated in the skeletal pathology of multiple MPSs [39]. A recent study using a different MPS-1 mouse model revealed that changes in extracellular matrix components of the skeleton are a major pathology of the disease which may be independent of GAG accumulation as decreased expression of type I collagen and other cartilaginous proteins occur before the histologic changes are visualized at the growth plate [36]. We further used Raman spectroscopy to evaluate the bone physiochemistry and demonstrated that female IDUA$^{-/-}$ mouse tibias have decreased mineral to matrix ratios and a decreasing trend in mineral to collagen ratios. It is unclear if the decreases in mineral to matrix and mineral to collagen ratios in the cortical bone are reflective of decreases in mineral content, or an increase in collagen content due to increases in collagen expression or decreases in the efficiency of collagen degradation by osteoclasts. The absence of differences in the bone mineral density distribution, as determined by quantitative back scattered scanning electron microscopy and cortical density, as determined by μCT analyses suggest that the ratio shifts are not due to alterations in mineral content. This finding is consistent with Wang et al. who reported that IDUA$^{-/-}$ and WT bone mineral density (BMD) were equivalent at 5 and 15 weeks of age, but by 35 weeks of age the IDUA$^{-/-}$ had greater BMD [15].

Defining the underlying mechanical properties of the skeletal abnormalities is the first step in elucidating the cellular and biochemical
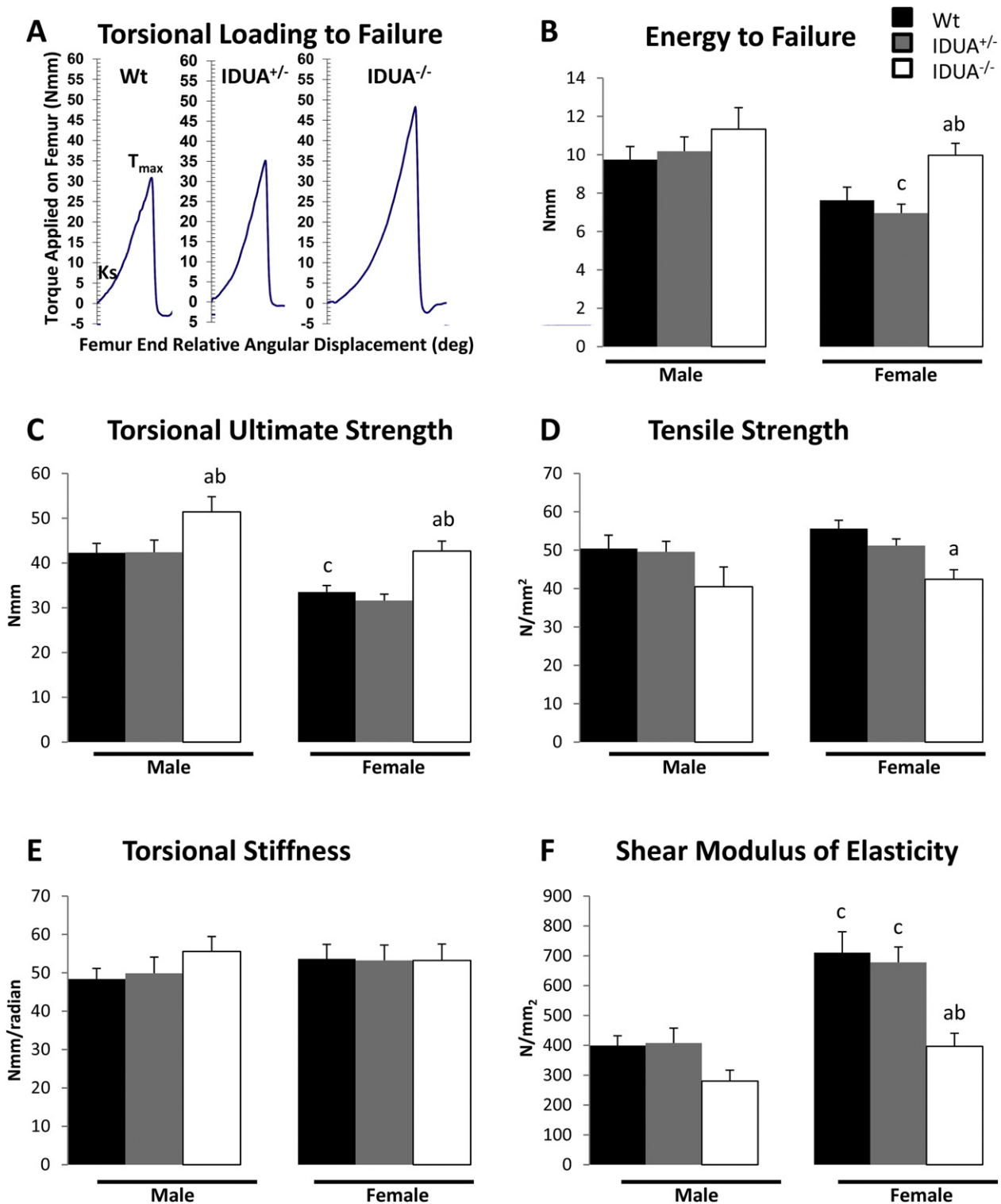
Fig. 6. Bone biomechanical integrity. A) Representative torsional loading to failure graphs from female Wt (*black bar*), IDUA$^{+/-}$ (*gray bar*), and IDUA$^{-/-}$ (*white bar*) femora. B) Energy to failure (U; the amount of energy the bone can absorb prior to fracture as measured by the area under the torque: angular displacement graph) of female IDUA$^{-/-}$ femora is increased compared to sex-matched Wt and IDUA$^{+/-}$ littermates. C) Torsional ultimate failure (T$_{max}$; the force at failure as measured by the peak of the torque: angular displacement curve) was increase in both male and female femora from IDUA$^{-/-}$ compared to sex-matched Wt and IDUA$^{+/-}$ littermates. D) Tensile strength (Su; the strength of the bone material as measured by subtracting the estimated strength contribution of the geometry component from the T$_{max}$) is decreased in femora from female IDUA$^{-/-}$ compared to sex-matched Wt littermates. E) Torsional stiffness (Ks; the stiffness of the bone as measured by the slope of the torque: angular displacement curve between 5 and 10 Nmm) is equivalent among all genotypes assessed. F) Shear modulus of elasticity (G; an estimate of the elasticity of the bone material as measured by the Ks—the estimated contribution of the geometry component) is reduced in femora from female IDUA$^{-/-}$ compared to sex-matched WT and IDUA$^{+/-}$ littermates. [a]$p \le 0.05$ compared to sex-matched Wt, [b]$p \le 0.05$ compared to sex-matched IDUA$^{+/-}$, [c]$p \le 0.05$ compared to genotype-matched male. Male Wt (n = 8), IDUA$^{+/-}$ (n = 6), and IDUA$^{-/-}$ (n = 7); Female Wt (n = 8), IDUA$^{+/-}$ (n = 8), and IDUA$^{-/-}$ (n = 5).

processes responsible for MPS I-H skeletal phenotype which will inform the improvement of current therapies and uncover potential therapeutic targets for the development of new therapies to further improve the bone quality of MPS I-H patients.

Acknowledgments

References

[1] A.H. Futerman, G. van Meer, The cell biology of lysosomal storage disorders, Nat. Rev. Mol. Cell Biol. 5 (7) (2004) 554–565 (Epub 2004/07/03).
[2] R.B. Lowry, D.H. Renwick, Relative frequency of the Hurler and Hunter syndromes, N. Engl. J. Med. 284 (4) (1971) 221–222 (Epub 1971/01/28).
[3] J. Wraith, Mucopolysaccharidoses. Emery and Rimoin's Principles and Practice of Medical Genetics, 2013 1–40.
[4] S.U. Walkley, Pathogenic cascades in lysosomal disease—why so complex? J. Inherit. Metab. Dis. 32 (2) (2009) 181–189 (Epub 2009/01/09).
[5] J.S. Weisstein, E. Delgado, L.S. Steinbach, K. Hart, S. Packman, Musculoskeletal manifestations of Hurler syndrome: long-term follow-up after bone marrow transplantation, J. Pediatr. Orthop. 24 (1) (2004) 97–101 (Epub 2003/12/17).
[6] P.G. de Oliveira, G. Baldo, F.Q. Mayer, B. Martinelli, L. Meurer, R. Giugliani, et al., Characterization of joint disease in mucopolysaccharidosis type I mice, Int. J. Exp. Pathol. 94 (5) (2013) 305–311 (Epub 2013/06/22).
[7] C. Taylor, P. Brady, A. O'Meara, D. Moore, F. Dowling, E. Fogarty, Mobility in Hurler syndrome, J. Pediatr. Orthop. 28 (2) (2008) 163–168 (Epub 2008/04/05).
[8] K.K. White, Orthopaedic aspects of mucopolysaccharidoses, Rheumatology 50 (Suppl. 5) (2011) v26–v33 (Epub 2012/01/11).
[9] M.H. van der Linden, M.C. Kruyt, R.J. Sakkers, T.J. de Koning, F.C. Oner, R.M. Castelein, Orthopaedic management of Hurler's disease after hematopoietic stem cell transplantation: a systematic review, J. Inherit. Metab. Dis. 34 (3) (2011) 657–669 (Epub 2011/03/19).
[10] M.N. Yasin, R. Sacho, N.J. Oxborrow, J.E. Wraith, J.B. Williamson, I. Siddique, Thoracolumbar kyphosis in treated mucopolysaccharidosis 1 (Hurler syndrome), Spine 39 (5) (2014) 381–387 (Epub 2014/02/28).
[11] J. Muenzer, J.E. Wraith, L.A. Clarke, International Consensus Panel on M, Treatment of mucopolysaccharidosis I. Mucopolysaccharidosis I: management and treatment guidelines, Pediatrics 123 (1) (2009) 19–29 (Epub 2009/01/02).
[12] G. Malm, B. Gustafsson, G. Berglund, M. Lindstrom, K. Naess, B. Borgstrom, et al., Outcome in six children with mucopolysaccharidosis type IH, Hurler syndrome, after haematopoietic stem cell transplantation (HSCT), Acta Paediatr. 97 (8) (2008) 1108–1112 (Epub 2008/05/03).
[13] L.A. Clarke, C.S. Russell, S. Pownall, C.L. Warrington, A. Borowski, J.E. Dimmick, et al., Murine mucopolysaccharidosis type I: targeted disruption of the murine alpha-L-iduronidase gene, Hum. Mol. Genet. 6 (4) (1997) 503–511 (Epub 1997/04/01).
[14] K. Ohmi, D.S. Greenberg, K.S. Rajavel, S. Ryazantsev, H.H. Li, E.F. Neufeld, Activated microglia in cortex of mouse models of mucopolysaccharidoses I and IIIB, Proc. Natl. Acad. Sci. U. S. A. 100 (4) (2003) 1902–1907 (Epub 2003/02/11).
[15] D. Wang, C. Shukla, X. Liu, T.R. Schoeb, L.A. Clarke, D.M. Bedwell, et al., Characterization of an MPS I-H knock-in mouse that carries a nonsense mutation analogous to the human IDUA-W402X mutation, Mol. Genet. Metab. 99 (1) (2010) 62–71 (Epub 2009/09/16).
[16] E.D. Kakkis, M.F. McEntee, A. Schmidtchen, E.F. Neufeld, D.A. Ward, R.E. Gompf, et al., Long-term and high-dose trials of enzyme replacement therapy in the canine model of mucopolysaccharidosis I, Biochem. Mol. Med. 58 (2) (1996) 156–167 (Epub 1996/08/01).
[17] N.M. Ellinwood, M.A. Colle, M.A. Weil, M.L. Casal, C.H. Vite, S. Wiemelt, et al., Bone marrow transplantation for feline mucopolysaccharidosis I, Mol. Genet. Metab. 91 (3) (2007) 239–250 (Epub 2007/05/08).
[18] Y. Zheng, N. Rozengurt, S. Ryazantsev, D.B. Kohn, N. Satake, E.F. Neufeld, Treatment of the mouse model of mucopolysaccharidosis I with retrovirally transduced bone marrow, Mol. Genet. Metab. 79 (4) (2003) 233–244 (Epub 2003/09/02).
[19] Y. Liu, L. Xu, A.K. Hennig, A. Kovacs, A. Fu, S. Chung, et al., Liver-directed neonatal gene therapy prevents cardiac, bone, ear, and eye disease in mucopolysaccharidosis I mice, Mol. Ther. 11 (1) (2005) 35–47 (Epub 2004/12/09).
[20] D. Wang, V. Belakhov, J. Kandasamy, T. Baasov, S.C. Li, Y.T. Li, et al., The designer aminoglycoside NB84 significantly reduces glycosaminoglycan accumulation associated with MPS I-H in the Idua-W392X mouse, Mol. Genet. Metab. 105 (1) (2012) 116–125 (Epub 2011/11/08).
[21] G. Gunn, Y. Dai, M. Du, V. Belakhov, J. Kandasamy, T.R. Schoeb, et al., Long-term nonsense suppression therapy moderates MPS I-H disease progression, Mol. Genet. Metab. 111 (3) (2014) 374–381 (Epub 2014/01/15).
[22] W.G. Beamer, K.L. Shultz, L.R. Donahue, G.A. Churchill, S. Sen, J.R. Wergedal, et al., Quantitative trait loci for femoral and lumbar vertebral bone mineral density in C57BL/6J and C3H/HeJ inbred strains of mice, J. Bone Miner. Res. Off. J. Am. Soc. Bone Miner. Res. 16 (7) (2001) 1195–1206 (Epub 2001/07/14).
[23] X. Yao, S.M. Carleton, A.D. Kettle, J. Melander, C.L. Phillips, Y. Wang, Gender-dependence of bone structure and properties in adult osteogenesis imperfecta murine model, Ann. Biomed. Eng. 41 (6) (2013) 1139–1149 (Epub 2013/03/29).
[24] M. Hahn, M. Vogel, M. Pompesius-Kempa, G. Delling, Trabecular bone pattern factor—a new parameter for simple quantification of bone microarchitecture, Bone 13 (4) (1992) 327–330 (Epub 1992/01/01).
[25] M.L. Bouxsein, S.K. Boyd, B.A. Christiansen, R.E. Guldberg, K.J. Jepsen, R. Müller, Guidelines for assessment of bone microstructure in rodents using micro-computed tomography, J. Bone Miner. Res. 25 (7) (2010) 1468–1486.
[26] R.C. Littell, P.R. Henry, C.B. Ammerman, Statistical analysis of repeated measures data using SAS procedures, J. Anim. Sci. 76 (4) (1998) 1216–1231 (Epub 1998/05/15).
[27] S.G. Carmer, M.R. Swanson, An evaluation of ten pairwise multiple comparison procedures by Monte Carlo methods, J. Am. Stat. Assoc. 68 (341) (1973) 66–74.
[28] W.J. Conover, R.L. Iman, Analysis of covariance using the rank transformation, Biometrics 38 (3) (1982) 715–724 (Epub 1982/09/01).
[29] C. Russell, G. Hendson, G. Jevon, T. Matlock, J. Yu, M. Aklujkar, et al., Murine MPS I: insights into the pathogenesis of Hurler syndrome, Clin. Genet. 53 (5) (1998) 349–361 (Epub 1998/07/11).
[30] J.E. Wraith, M. Scarpa, M. Beck, O.A. Bodamer, L. De Meirleir, N. Guffon, et al., Mucopolysaccharidosis type II (Hunter syndrome): a clinical review and recommendations for treatment in the era of enzyme replacement therapy, Eur. J. Pediatr. 167 (3) (2008) 267–277 (Epub 2007/11/27).
[31] M. Aldenhoven, J.J. Boelens, T.J. de Koning, The clinical outcome of Hurler syndrome after stem cell transplantation, Biol. Blood Marrow Transplant. 14 (5) (2008) 485–498 (Epub 2008/04/16).
[32] L.E. Polgreen, J. Tolar, M. Plog, J.H. Himes, P.J. Orchard, C.B. Whitley, et al., Growth and endocrine function in patients with Hurler syndrome after hematopoietic stem cell transplantation, Bone Marrow Transplant. 41 (12) (2008) 1005–1011 (Epub 2008/02/19).
[33] R.E. Stevenson, R.R. Howell, V.A. McKusick, R. Suskind, J.W. Hanson, D.E. Elliott, et al., The iduronidase-deficient mucopolysaccharidoses: clinical and roentgenorgraphic features, Pediatrics 57 (1) (1976) 111–122 (Epub 1976/01/01).
[34] D.J. Rowan, S. Tomatsu, J.H. Grubb, A.M. Montano, W.S. Sly, Assessment of bone dysplasia by micro-CT and glycosaminoglycan levels in mouse models for mucopolysaccharidosis type I, IIIA, IVA, and VII, J. Inherit. Metab. Dis. 36 (2) (2013) 235–246 (Epub 2012/09/14).
[35] S. Abreu, J. Hayden, P. Berthold, I.M. Shapiro, S. Decker, D. Patterson, et al., Growth plate pathology in feline mucopolysaccharidosis VI, Calcif. Tissue Int. 57 (3) (1995) 185–190 (Epub 1995/09/01).
[36] J.M. Heppner, F. Zaucke, L.A. Clarke, Extracellular matrix disruption is an early event in the pathogenesis of skeletal disease in mucopolysaccharidosis I, Mol. Genet. Metab. 114 (2) (2015) 146–155 (Epub 2014/11/21).
[37] S. Wilson, S. Hashamiyan, L. Clarke, P. Saftig, J. Mort, V.M. Dejica, et al., Glycosaminoglycan-mediated loss of cathepsin K collagenolytic activity in MPS I contributes to osteoclast and growth plate abnormalities, Am. J. Pathol. 175 (5) (2009) 2053–2062 (Epub 2009/10/17).
[38] A. Pievani, I. Azario, L. Antolini, T. Shimada, P. Patel, C. Remoli, et al., Neonatal bone marrow transplantation prevents bone pathology in a mouse model of mucopolysaccharidosis type I, Blood 125 (10) (2015) 1662–1671 (Epub 2014/10/10).
[39] D.A. Stevenson, K. Rudser, A. Kunin-Batson, E.B. Fung, D. Viskochil, E. Shapiro, et al., Biomarkers of bone remodeling in children with mucopolysaccharidosis types I, II, and VI, J. Pediatr. Rehabil. Med. 7 (2) (2014) 159–165 (Epub 2014/08/07).
[40] C. Niyibizi, D.R. Eyre, Structural characteristics of cross-linking sites in type V collagen of bone. Chain specificities and heterotypic links to type I collagen, Eur. J. Biochem. 224 (3) (1994) 943–950 (Epub 1994/09/15).
[41] S. Viguet-Carrin, P. Garnero, P.D. Delmas, The role of collagen in bone strength, Osteoporos. Int. 17 (3) (2006) 319–336 (Epub 2005/12/13).